



Physical simulation of investment casting for GTD-222 Ni-based superalloy processed by controlled cooling rates

Jiangping Yu^{1,2} · Donghong Wang^{1,3,4} · Dayong Li^{2,4} · Ding Tang² · Guoliang Zhu^{1,3} · Anping Dong^{1,3} · Da Shu^{1,3,4} · Yinghong Peng²

Received: 6 May 2019 / Accepted: 24 October 2019 / Published online: 13 November 2019
© Springer-Verlag London Ltd., part of Springer Nature 2019

Abstract

The influence of the solidification process parameters on the microstructure is still identified by the trial and error method. It is common practice to perform multiple casting tests to defecate the optimum process parameters for high-quality casting parts. In order to establish the solidification-microstructure relationship, a high-efficiency experimental method is proposed to accelerate the speed of finding the optimum casting process parameters by the controlled cooling rate of 0.25 °C/s, 1 °C/s, 5 °C/s, and 10 °C/s, respectively. It demonstrated that the physics simulation can successfully predict the microstructure of the GTD-222 Ni-based superalloy casting and the relationship between the secondary dendrite arm spacing (SDAS) and cooling rate is $\lambda_2 = 76.4747(GV)^{-0.2926}$. The response behavior of secondary dendrite arm spacing is sensitive to the change of solidification parameters. Moreover, the microhardness tends to decrease along the axial direction as well. The relationships between the temperature gradient, cooling rate, and microstructure are discussed as well. The results also show that the prior model of the numerical simulation and the physical simulation of the high-efficiency experiment design can reproduce the conventional casting conditions and the high-efficiency experiment can be applied to other casting studies of all kinds for the enhancement of time- and cost-saving.

Keywords GTD-222 Ni-based superalloy · Microstructure cooling rate · Temperature gradient · High-efficiency experiment

1 Introduction

Investment casting, as an advanced near net shape technology with superior surface smoothness and dimensional exactitude, is particularly suitable for the casting of intricate interface-

cavity structures. In the past 10 years, investment casting has been developed rapidly all over the world and is widely applied to the aero-engine and gas turbine components such as cylinder blocks, turbine blades [1–3], etc. These parts are usually serviced under extreme conditions (i.e., high temperature and high pressure) since they are made of nickel-based alloys and served at high temperatures for its high strength, good oxidation resistance, and creep resistance. Hence, a new cast nickel-base nozzle alloy named GTD-222 Ni-based superalloy emerged and was considered to be a replacement for cobalt-base alloy FSX-414 due to its good castability, better creep resistance, and oxidation resistance [4]. Furthermore, the GTD-222 superalloy is considered to be a latent applicant for large, complicated thin-walled castings with high-temperature resistance in next-generation aircraft generators.

Still, numerous efforts and time have been put into the development of the investment casting process to build multiple shape parts for producers in the form of experiments as well as numerical simulation. The casting trials and simulations are typically conducted to discover the excellent casting parameters for fabrication of high-quality outputs. Wang [5] found that the uniform distribution of TiN particles strongly

✉ Donghong Wang
wangdh2009@sjtu.edu.cn

Dayong Li
dyl@sjtu.edu.cn

¹ Shanghai Key Lab of Advanced High-Temperature Materials and Precision Forming, School of Materials Science and Engineering, Shanghai Jiao Tong University, Shanghai 200240, China
² State Key Laboratory of Mechanical System and Vibration, School of Mechanical Engineering, Shanghai Jiao Tong University, Shanghai 200240, China
³ State Key Laboratory of Metal Matrix Composites, School of Materials Science and Engineering, Shanghai Jiao Tong University, Shanghai 200240, China
⁴ Materials Genome Initiative Center, Shanghai Jiao Tong University, 800 Dong Chuan Road, Shanghai 200240, China

affects the microstructure as well as the mechanical properties of TiN/IN718C composites during investment casting. Kartavykh [6] studied the formation of equiaxed grains under the directional solidification by changing the process condition and the mental dopant. Aveson [7] studied the deformation of the dendrites in investment castings and quantified the misorientation by EBSD, it turned out that the defects were produced by the bending movements through different thermal shrinkage. Li [8] utilized the ProCAST software to simulate the porosity of TiAl based alloy blade and the optimized processing result indicated that the porosity could be reduced by preheating the shell, which means that the reliability and precision between simulation and experiment were well combined. Yang [9] investigated the gravity and centrifugal investment casting processes by ProCAST software and pointed out that the fast cooling rate was the crucial factor to refine the microstructure where a large number of γ segregation occurred simultaneously in Nb-TiAl alloy.

In spite of numerical simulation for investment casting, physical simulation can also well predict the thermal distribution of complex structure castings and defects in the casting process, and therefore reduces the cost and time for production. Bergman [10] firstly made the thermal simulator to simulate the actual manufacturing process of material processing. Lewandowski [11] conducted thermal compression experiments on IN718 through a Gleeble physical simulator, further characterizing the mechanical response behavior of the IN718 superalloy in the solid and semi-solid state. Rahimian [12] conducted a double heat-treatment via physical simulation to explore the microstructure and hardness evolution of MAR-M247 superalloy and further discussed the relationship between material processing, microstructure, and microhardness.

For castings, the cooling rate varies much along the surface to the center of the mold, which means that a temperature gradient occurs in the different area (such as thin and thick-wall) of the casting. However, when the temperature gradient exists, the cooling rate is not a single factor affecting the growth of the microstructure, but also related to the growth rate of solidification interface [13, 14].

Alloys for given components, the temperature gradient (G) and solidification rate (V) are the crucial parameters governing the morphology of the alloy together with solidification behavior. In addition, the inherent thermodynamic properties of the alloy and the extrinsic factors such as the heat flux of the melt are affecting the relationship between G and V [15, 16]. Generally, investigating the relationship between solidification parameters and microstructural growth needs to be realized by numerous investment casting experiment. However, such a strategy is time-consuming and expensive, which is not conducive to mass production. High-efficiency experiment in investment casting modeling is another way to ascertain the optimum process parameters for doing multiple sets of experiments [17]. Makihata [18] proposed a new method in printing machine for the printing speed was five times faster than before. Kirklın [19] used high-efficiency approaches to search for high-strength precipitation-hardened systems. Sáfrán [20] proposed a high-flux combination technique to realize the preparation and detection of two-component thin-film materials on a single transmission sample. Li [21] studied the influence of process parameters including initial temperature, area reduction, and rolling speed on the cross wedge of TC6 alloy, it turned out that the best rolling speed should be 8 r/min and further discussed the influence of the parameters on the alpha phase.

Recent progress in science and technology contributes to researchers for producing the physical simulation of casting processes and building the relationship between parameters and microstructure. Different parameters such as cooling rate have different influences on the microstructure of the same casting parts, therefore, inducing the versatile mechanical performance simultaneously. However, bringing such a relationship into reality one by one is not possible in a short time with low costs. In this study, a novel high-efficiency experimental method is proposed to investigate the solidification behavior with the occurrence of G and V , leading to the acquisition of the relationship between solidification parameters and microstructure during the investment casting process. This paper aims to present a novel

Fig. 1 **a** The actual turbine guide for investment casting; **b** a half 3D model of the turbine guide; **c** the various spots located in cross-section for obtaining the local cooling rate

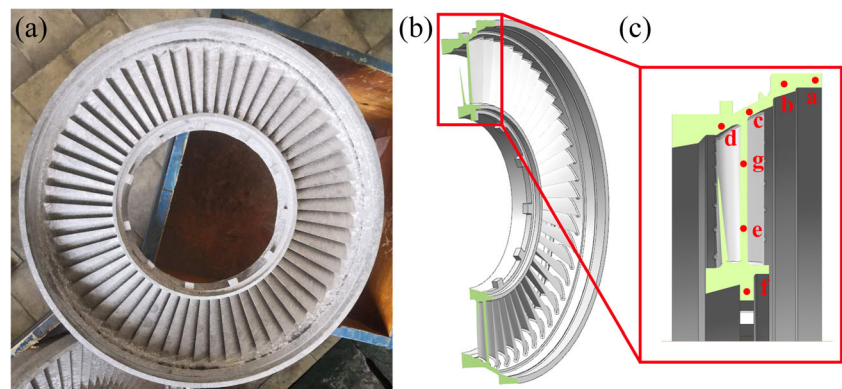
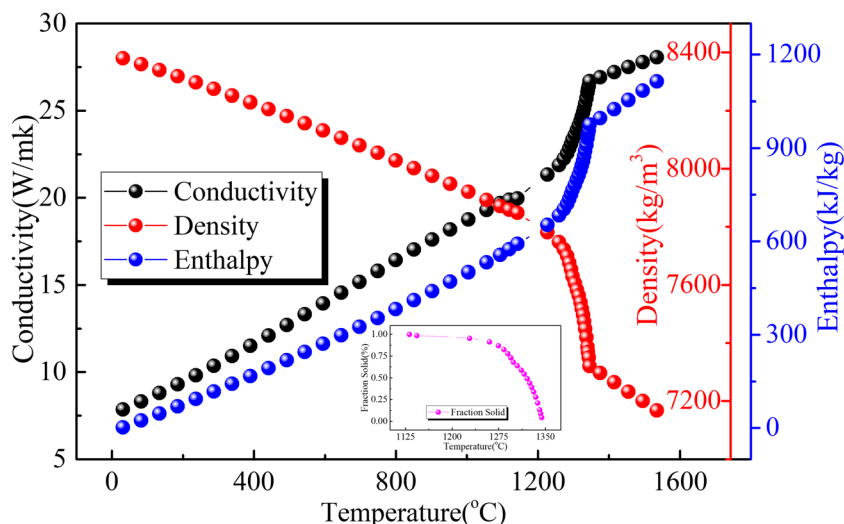


Fig. 2 The thermodynamic properties of the GTD-222 superalloy



scientific method to investigate the solidification-microstructure relationship. The technical routes are as follows: (1) the construction of actual castings in UG software; (2) the prior model of numerical simulation in ProCAST and (3) the physical simulation based on high-efficiency experiment design. All the experiments in this paper are based on investment casting technology with a feature part of the turbine guide of GTD-222 Ni-based superalloy.

2 Material and methods

2.1 The numerical simulation for investment casting parts

The casting used in this research was the turbine guide as shown in Fig. 1. After the three-dimension model of the turbine guide was established in UG NX10.0, it was imported

into ProCAST software. Subsequently, the surface mesh and the volume mesh were generated by Visual-Mesh and the mesh size was 3 mm. Then, the shell was selected from a fused silica shell and preset to a uniform thickness of 6 mm. At the same time, the pouring temperature was 1500 °C, and the preheating temperature of the shell was 1000 °C for the turbine guide casting. Additionally, all the thermodynamic properties of the alloy utilized in the numerical simulation were obtained from the material database of ProCAST calculated before and were seen in Fig. 2.

For the turbine guide casting, a few feature points from the cross-section was selected as shown in Fig. 1c. The variation of the temperature of the selected feature points was presented in Fig. 3. The temperature in the solid-liquid phase region showed a linear relationship from different thickness so as the cooling rate could be obtained by the linear fitting. The results indicate that the cooling rate of feature points ranges from 0.32 to 4.22 °C/s, which means the cooling speed of the blades was larger than that of the inner ring and outer ring.

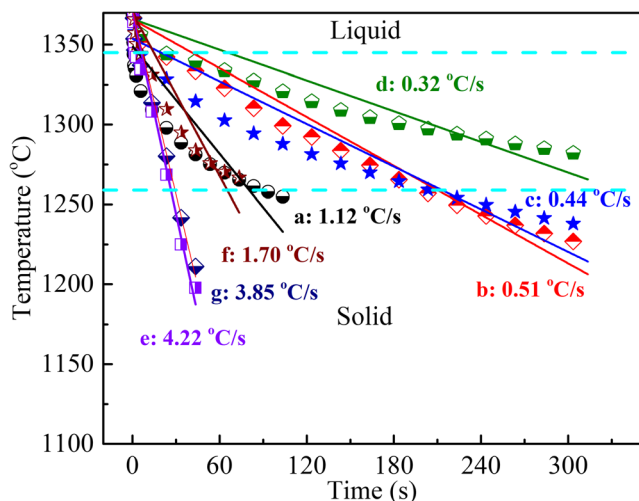


Fig. 3 The schematic diagram of linear-fitting of the curve for various local cooling rates in the solid-liquid phase region

2.2 Physical simulation experiment

2.2.1 Material

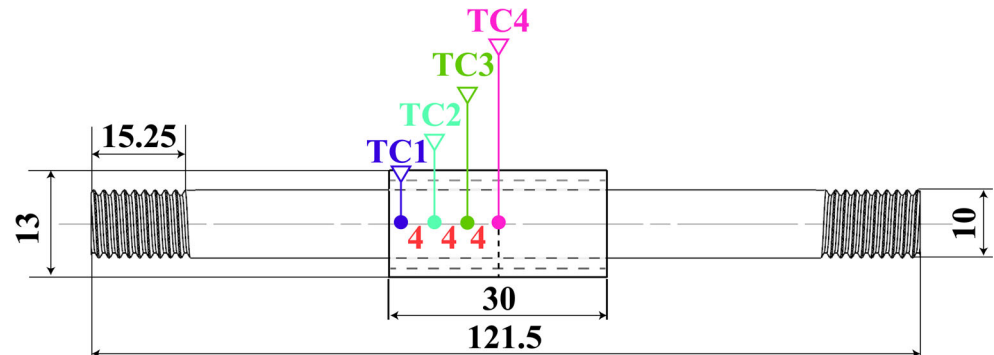
The material used in this investigation is a GTD-222 Ni-based superalloy, and the chemical composition of the material is presented in Table 1.

2.2.2 Experimental procedures

The cylindrical testing sample with the diameter of 10 mm and the length of 121.5 mm is cut from the ingot (provided by Central Iron & Steel Research Institute (CISRI, China) and the diameter of it was 100 mm and the height 150 mm.) by linear cutting. The sample was grounded by sandpaper to remove the surface oxide layer and subsequently washed in

Table 1 Chemical composition of the GTD-222 nickel-based superalloy (wt.%)

Element	C	Cr	Nb	Ti	W	Al	B	Zr	Co	N	O	S	Ni
Content	0.08–0.12	22.2–22.8	0.7–0.9	2.2–2.4	1.8–2.2	1.01–1.03	0.002–0.007	0.005–0.02	18.5–19.5	≤0.01	≤0.005	≤0.007	Bal.

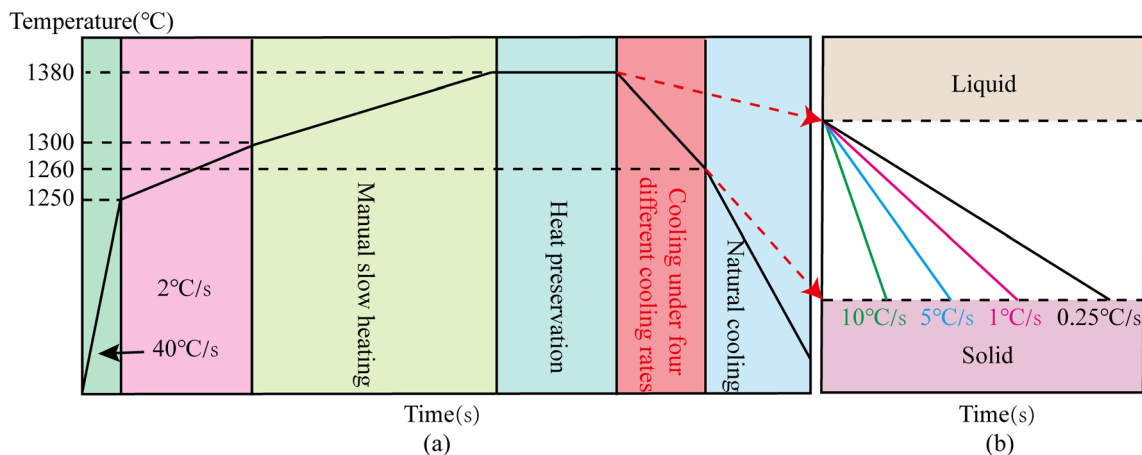
Fig. 4 Dimensions of melt/solidification test specimens and the distribution of thermocouples welded on it

acetone for ultrasonic cleaning. Finally, the sample was machined to the standard sample as the Gleeble device required, and the processing dimension is shown in Fig. 4.

Four different positions located from the center at 0 mm, 4 mm, 8 mm, and 12 mm in cross-section were selected. Hereafter, the R-type Pt-Rh thermocouples were welded on the surface of the four selected positions of the specimen marked as TC4, TC3, TC2, and TC1 (seen in Fig. 4 with colorful lines). Since the sample was symmetrical in the center, the thermocouples were welded on one side of the sample. The Gleeble 3800 simulator is based on temperature control with an accuracy of ± 0.1 °C so that the real-time temperature change of the sample can be acquired accurately. Furthermore, the samples are coated with quartz tubes ($\Phi 13 \times 30$, unit: mm) for the sake of thermal dissipation in the radial direction. At the same time, high-temperature cement was applied to the thermocouple welding area to prevent the alloy from falling off due to the thermal expansion and contraction of the

sample. Finally, the sample was fixed by a pair of copper clamps in Gleeble chamber.

According to the results of numerical simulation discussed above and considering to obtain the maximum temperature gradient for better observation of its effect on the microstructure [22], four suitable cooling rates, 0.25 °C/s, 1 °C/s, 5 °C/s, and 10 °C/s, were selected in this study. The detailed Gleeble-processing steps for melting/solidification experiments are presented in Fig. 5. Firstly, the sample was heated to 1250 °C at a rate of 40 °C/s, and then in the range of 1250 °C–1300 °C, the heating rate was reduced to 2 °C/s. After that, the temperature was raised manually and heated to 1380 °C at a very slow rate until the signs of melting were observed, indicating that the sample temperature was already in the liquids. So, the heating needed to stop immediately and kept it warm for 10 seconds. Subsequently, there were two crucial steps to be set up: the first step was programmed to cool down to 1260 °C at four different cooling rates of 0.25 °C/s, 1 °C/s, 5 °C/s,

**Fig. 5** Gleeble processing curve: **a** overall process; **b** four different cooling rates: 0.25 °C/s, 1 °C/s, 5 °C/s, and 10 °C/s from right to left

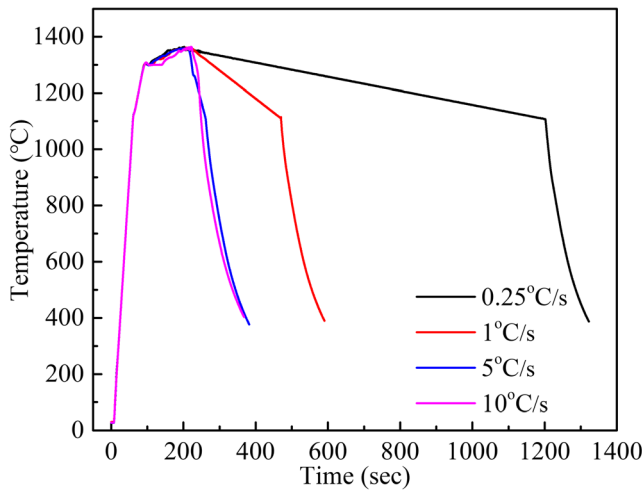


Fig. 6 The actual process curve of Gleeble samples in midsection under different cooling rates

and 10 °C/s. Then the second step was naturally cooled to room temperature. During the experiment, argon was injected into the chamber to avoid oxidizing. In case of shrinkage defects, the displacement feeding amount is set in advance in the execution procedure. Each experiment was repeated three times to ensure a reliable and repeatable experiment.

The samples utilized for microstructure characterization were cut from the welding area (TC1, TC2, TC3, and TC4, as seen in Fig. 4 with color lines); the size of it was $\Phi 10 \times 2$ mm. To reveal the dendritic microstructure, the flake-shape sample was corroded by a mixture of 50 mL C_2H_5OH , 50 mL HCl , 3.5 mL H_2SO_4 , and 15 g $CuSO_4$ after grinding and polishing. The microstructure was adopted by Leica DM-4000 M optical microscope (OM). Microhardness is obtained by the Vickers hardness test later. The measurement of SDAS is achieved by counting the number of secondary arms over a length on at least one hundred well-defined trunks.

2.2.3 Calculation of cooling rate, temperature gradient, and solidification rate

Firstly, the cooling rate of different parts of the sample can be expressed as follows:

$$R = dT/dt \tag{1}$$

After selecting one or more time points, the four welded thermocouples can acquire the individual temperature along the axial direction at every time point. As a

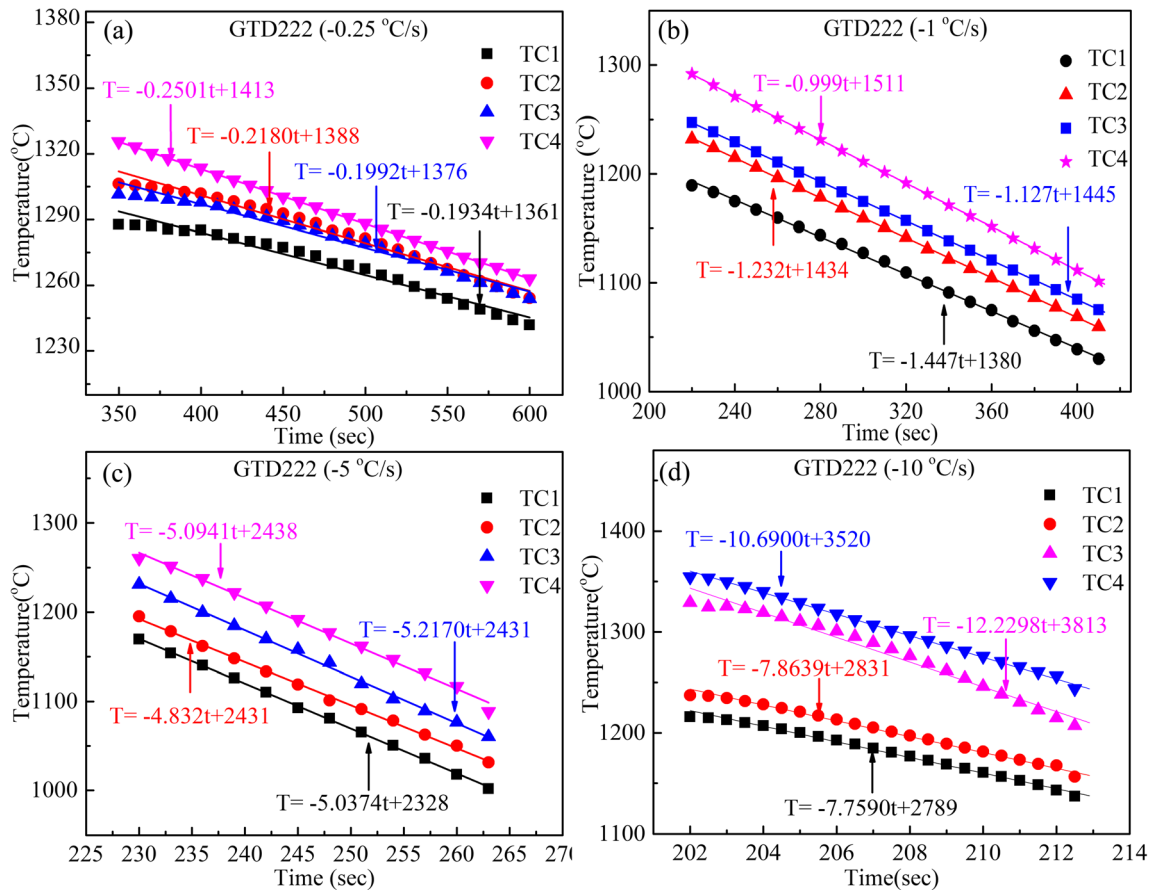


Fig. 7 The temperature evolution in the liquid-solid zone along the axial direction based on various controlling of cooling rate: **a** 0.25 °C/s, **b** 1 °C/s, **c** 5 °C/s, and **d** 10 °C/s, respectively

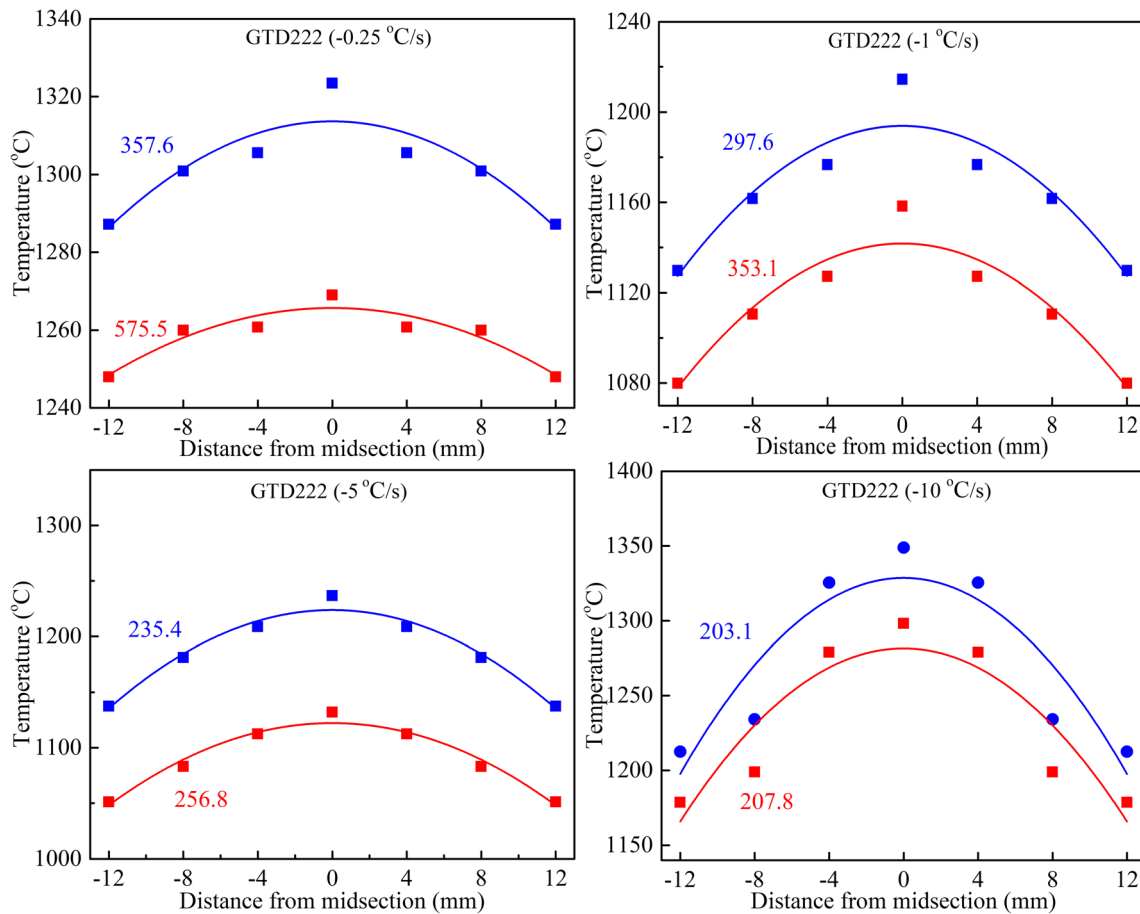


Fig. 8 Temperature distribution in the samples cooled at (a) 0.25 °C/s, (b) 1 °C/s, (c) 5 °C/s, and (d) 10 °C/s, respectively

result, the temperature-distance (T-D curve) can be acquired by the fitting of a multi-curve via a polynomial function as follows:

$$T = aD^2 + bD + c \tag{2}$$

The constants a, b, and c can be easily determined from the fitting lines, while the D is the distance along the axial direction. As for the temperature gradient, the derivation of the formula (2) can be obtained as follows:

$$G = dT/dD = 2aD + b \tag{3}$$

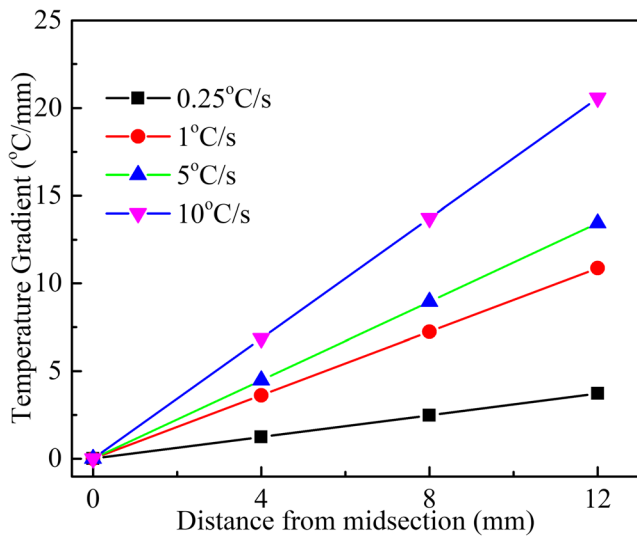


Fig. 9 Temperature gradient evolution along the axial direction with different cooling rates

Table 2 Summary of the temperature gradient(G), true cooling rate(R), and solidification rate(V) in different sections along the melted/solidified samples

Cooling rate	Distance (mm)	R (°C/s)	G (°C/mm)	V (μm/s)
0.25	0	0.25	-	-
	4	0.20	1.24	161.29
	8	0.22	2.48	88.71
	12	0.19	3.72	51.08
1	0	1.00	-	-
	4	1.13	3.62	312.15
	8	1.23	7.25	169.66
	12	1.45	10.87	133.39
5	0	5.09	-	-
	4	5.22	4.48	1169.18
	8	4.83	8.96	539.06
	12	5.04	13.44	375.00
10	0	10.69	-	-
	4	12.23	6.86	1782.80
	8	7.86	13.72	572.89
	12	7.76	20.57	377.25

For the existing cooling rate (R) and temperature gradient (G), the solidification rate (V) of GTD-222 alloy in the solid-liquid zone can be obtained, and the solidification rate V can be expressed as [23]:

$$V = R/G \quad (4)$$

3 Results and discussions

The actual temperature curve of the sample in the thermocouples welding area is shown in Fig. 6. Though the high temperature is different to control, the result is more likely to the heating process curve that has been set before.

3.1 Temperature gradients

The actual temperature-time curves (T - t) of GTD-222 Ni-base superalloy extracted from the solid-liquid region are presented in Fig. 7. Through those colorful points, the actual cooling rate can be easily estimated with the aid of spot-welded thermocouple. It turns out that the cooling rates (namely, the slope of

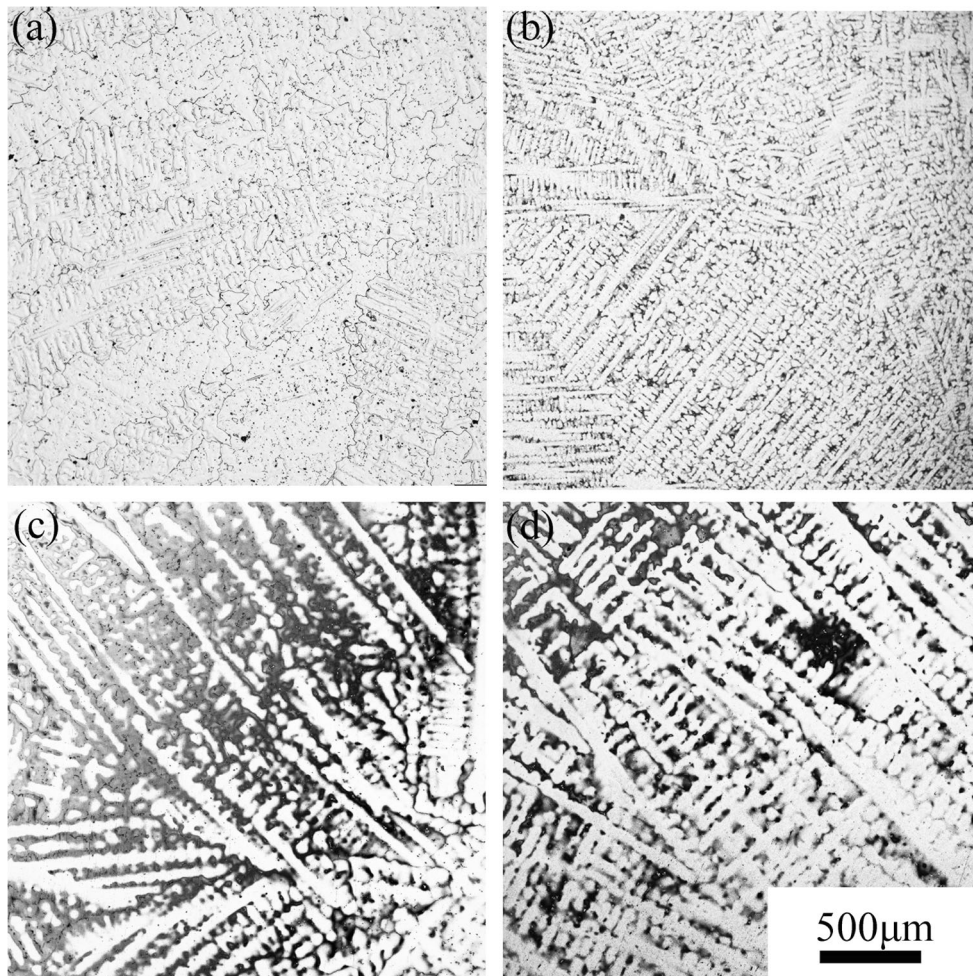
each fitting line.) in the solid-liquid region are close to a preset value, making it clear that the control of the temperature in Gleeble is much more accurate and reliable.

Two-time points are selected at each cooling rate to obtain the temperature along the axial direction. Fig. 8 shows the temperature change of the sample obtained along the axial direction at the same time point (blue and red color). It turns out that those points are more likely to distribute around the quadratic function lines.

As a result, the average temperature gradient (G) can be extracted from Fig. 8 and is shown in Fig. 9. The value of each point is the average of two different timesteps that previously selected. It turns out that the increase of the controlled cooling rate lead to an increase of the temperature gradient. The gradient is much steeper in the case of the higher cooling rate. Additionally, at the cooling rate of 10 °C/s, it increased more rapidly than that of 0.25 °C/s. When the controlled cooling rate gets to 10 °C/s, the temperature gradient of the sample can correspondingly reach 20.57 °C/mm.

Table 2 lists the summary of the cooling rate (R), temperature gradient (G , calculated by formula 3), and solidification rate (V , calculated by formula 4) of GTD-222 alloy in solid-

Fig. 10 The dendritic microstructure of the Gleeble samples cooled at 0.25 °C/s from the transversal section at **a** 0 mm, **b** 4 mm, **c** 8 mm, and **d** 12 mm, respectively



liquid phase zone. The range of the temperature gradient and the solidification rates are 1.24 to 20.57 °C/mm and 0.05 to 1.78 mm/s, which is obtained by the high-efficiency experiment. It can be seen that the cooling rate (R) and the temperature gradient (G) will gradually increase as the distance (D) from the center increase simultaneously. However, the solidification rate (V) appears to the contrary. It was observed that the R/G value greatly changed at the same cooling rate, which means the solidification rate was changing rapidly. In other words, the solidification interface moved fast from the micro perspective, resulting in the significant change of the microstructure.

3.2 The characterization of microstructure

In general, the secondary dendrite arm spacing (SDAS) is one of the primary structures of solidified castings, which is crucial to mechanical performance. Especially, the size of SDAS directly affects the mechanical properties, the micro-segregation, the distribution of the second phase, and the micro-porosity of the casting. The SDAS is determined by many factors, especially the temperature gradient (G), the

solidification rate (V), and cooling rate (R) as well [24]. Many studies have been carried out to investigate the interaction of G, V, and R on SDAS [25–27].

The cross-sectional microstructure of GTD-222 conducted by a high-efficiency experiment method under different cooling rates is obtained and presented in Fig. 10, 11, 12, 13. The impacts of temperature gradient on the dendritic-like microstructure of GTD-222 Ni-based superalloy in the Gleeble samples gradually emerge. The results confirm that solidification parameters, such as R as well as G, decree the microstructural morphology (seen in Fig. 10). From the sequential pictures (seen in Fig. 10, 11, 12, 13), the SDAS decrease with an increasing cooling rate which is in a good agreement with the results reported earlier by Zhang [28] and many other research groups [29, 30]. As a result, increasing cooling rates can lead to the refinement of the microstructure. The growth of SDAS is influenced by the local solidification time, which means enough contact with liquid helps a better secondary branch since the solute diffusion coefficient is larger than that in the solid.

Moreover, it demonstrates that primary dendrite arm spacing (SDAS) of the disordered arrangement will gradually

Fig. 11 The dendritic microstructure of the Gleeble samples cooled at 1 °C/s from the transversal section at **a** 0 mm, **b** 4 mm, **c** 8 mm, and **d** 12 mm, respectively

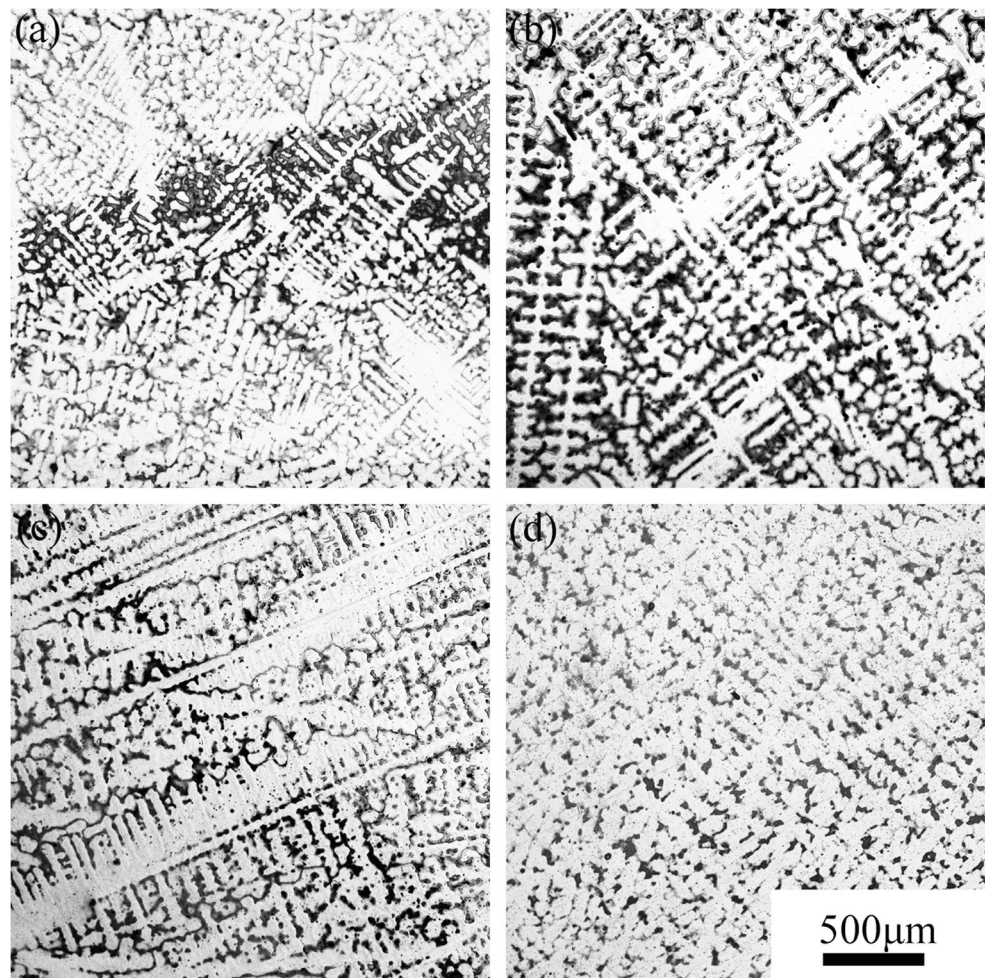
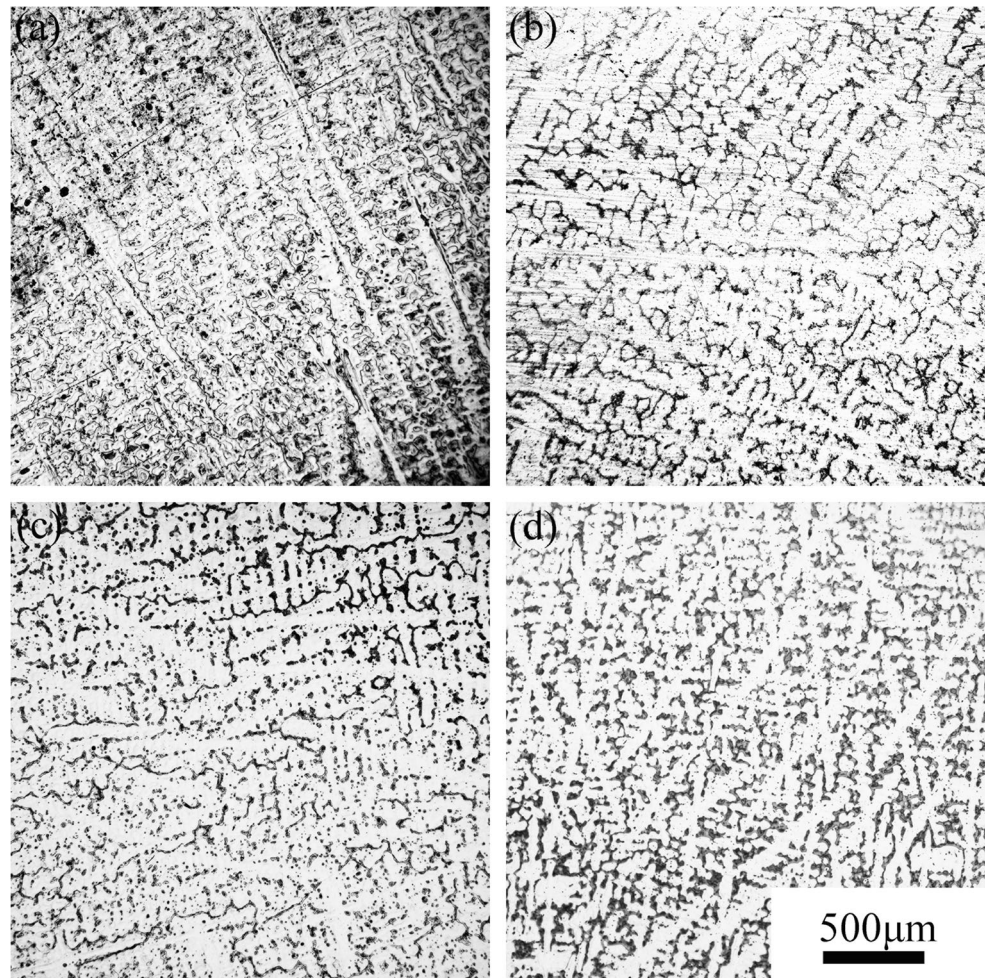


Fig. 12 The dendritic microstructure of the Gleeble samples cooled at 5 °C/s from the transversal section at **a** 0 mm, **b** 4 mm, **c** 8 mm, and **d** 12 mm, respectively



grow parallel to each other with the increase of the temperature gradient. While the primary dendrite arm spacing (PDAS) increase, the secondary dendrite arm spacing (SDAS) will increase simultaneously. The reason is that with the increase of the temperature gradient, the distribution of solute atoms between the dendrites inhibits the regeneration of secondary dendrites, resulting in secondary dendrite coarsening. Consequently, the solidification rate is blamed for the SDAS coarsening. With the increase of solidification rate, the response behavior of SDAS is changing sharply. Additionally, for those that are uneven, which means the intersection angle occurs, the growth of SDAS has been terminated since the diffusion of the solute between the dendrites is favorable to the well-aligned structure.

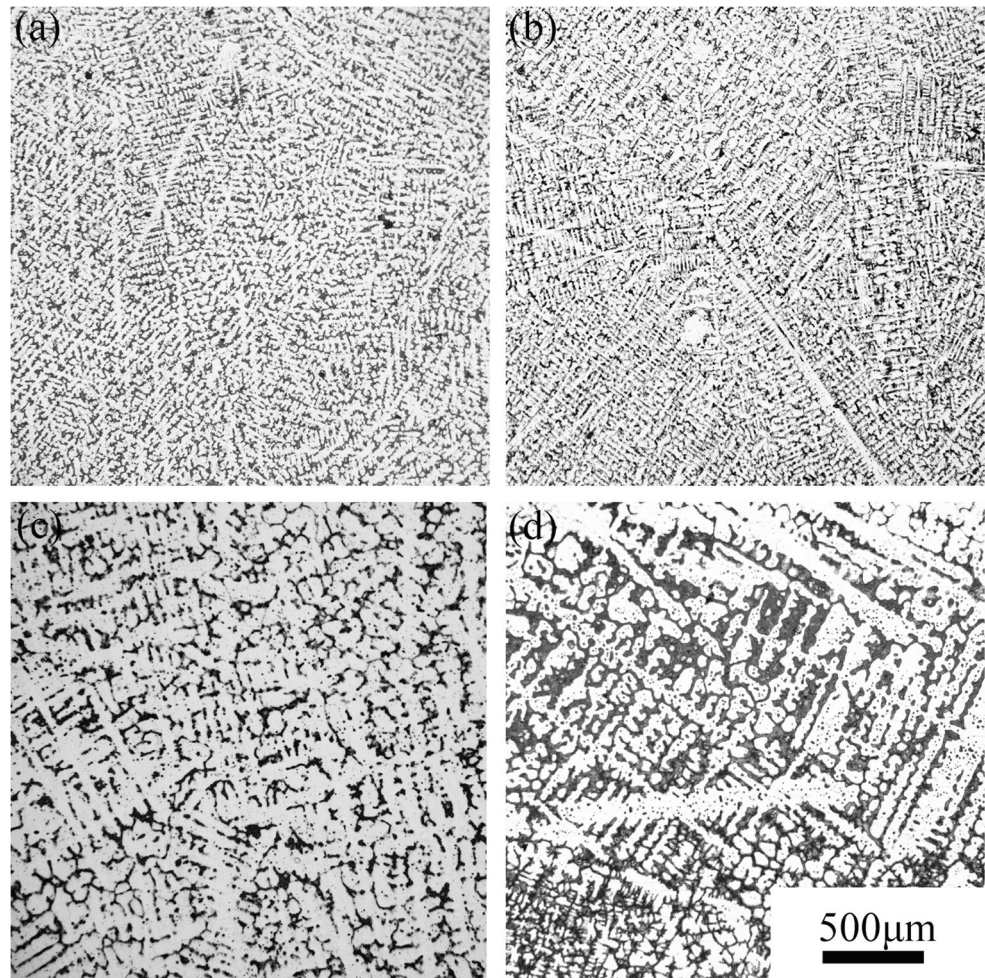
Fig 13(a–d) illustrates the typical structure of SDAS in GTD-222 Ni-based superalloy after melting/solidification experiments displaying some well-aligned SDAS; on the contrary, the secondary dendrites are disordered. Along the axial direction, there is an obvious transformation from the dendritic structure (Fig. 13a, b) to cellular growth (Fig. 13c, d) at a cooling rate of 10 °C/s

which means the microstructure is changed with the thermal gradient increasing.

Fig 14(a, b) shows the variation of the secondary dendrite arm spacing (SDAS) and microhardness of GTD-222 alloy under different cooling rate along the axial direction. It turns out that the maximum SDAS is 71.90 μm at the section of 12 mm from the midsection, almost 1.5 times as much as it is in the center, which is also accounting for the sharply changing of SDAS while the thermal gradient exists. What's more, it can be seen that the SDAS trend to decrease with the cooling rates increasing at the same section from the center of the sample. Apparently, the hardness of the Victorinox is decreased along the axial direction because it is mainly governed by the carbide. One possible reason may account for this phenomenon. The carbide could not precipitate in time with the sharp increment of the temperature gradient.

The relationship between the secondary dendrite arm spacing (SDAS) and the temperature gradient (G) have been widely studied before [31]. Generally, the growth of the secondary dendrite is accompanied by the grain coarsening, which seriously affects the secondary dendrite arm spacing (SDAS).

Fig. 13 The dendritic microstructure of the Gleeble samples cooled at 10 °C/s from the transversal section at **a** 0 mm, **b** 4 mm, **c** 8 mm, and **d** 12 mm, respectively



Melo et al. [32] quantitatively described the relationship between solidification parameters and secondary dendrite arm spacing (SDAS) as follows:

$$\lambda_2 = 6.8 \left(\frac{D\Gamma}{GVK} \right)^{1/3} \quad (5)$$

It indicates that the SDAS and the cooling rate ($R = G \times V$) obey the rule: $\lambda_2 \propto R^{-1/3}$. Figure 15 presents the relationship between the SDAS and (a) solidification rate and (b) cooling rate, respectively. Fig 15(a) shows the SDAS of GTD-222 in relation to solidification rate (V) has low convergence and R^2 is 0.0941. However, the SDAS corresponding to cooling rate

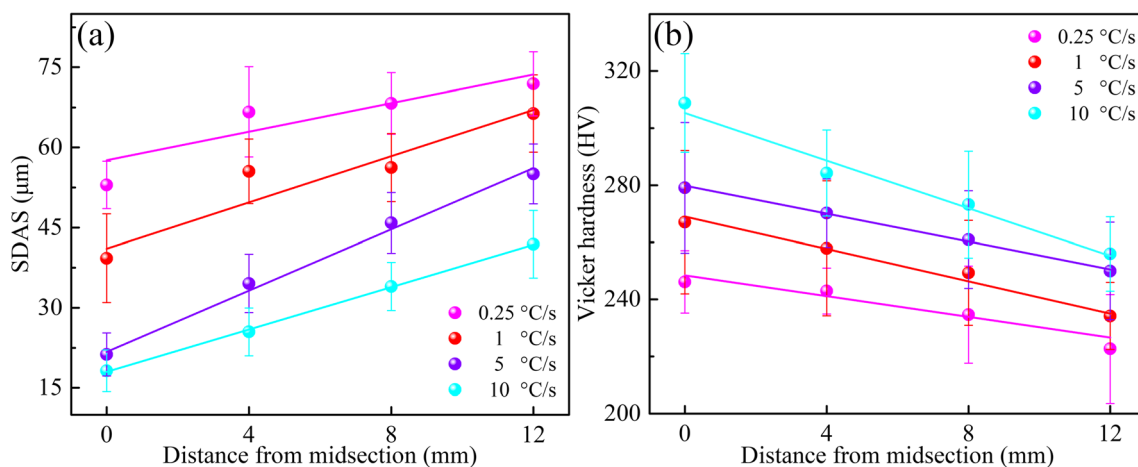


Fig. 14 The distribution of **a** SDAS and **b** Vickers hardness along the axial direction at 0 mm, 4 mm, 8 mm, and 12 mm, respectively

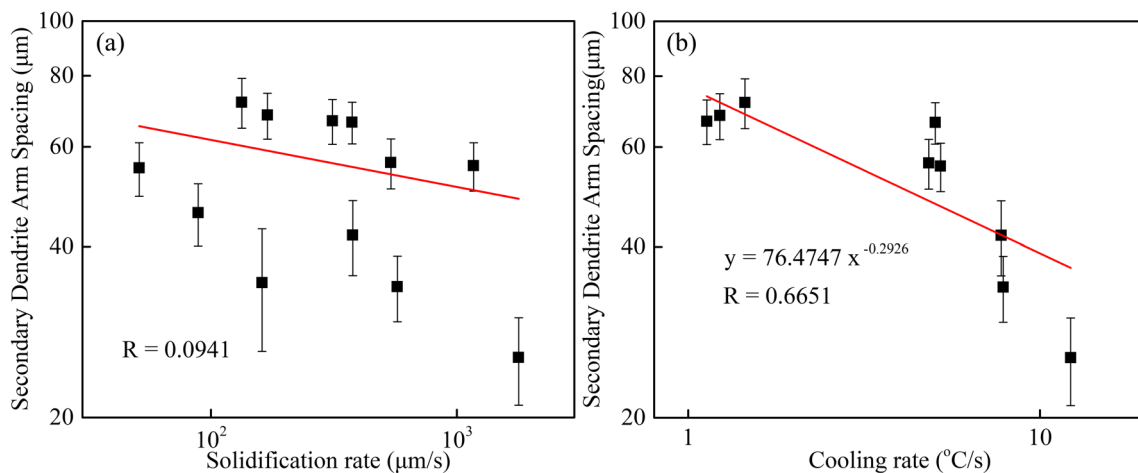


Fig. 15 The variation of SDAS with **a** solidification rate; **b** cooling rate

R has a higher convergence and R^2 has a value of 0.6651. The regression equation for SDAS is:

$$\lambda_2 = 76.4747(GV)^{-0.2926} \quad (6)$$

4 Conclusions

In this paper, a physical simulation has been conducted to establish the solidification-microstructure relationship of GTD-222 superalloy via a new high-efficiency method. The following conclusions can be drawn:

1. The range of the cooling rate is 0.32 to 4.22 °C/s, which is acquired from the turbine guide by simulation. Furthermore, the range of the temperature gradient and the solidification rates are 1.24 to 20.57 °C/mm and 0.05 to 1.78 mm/s, which is obtained by the high-efficiency experiment.
2. The physics simulation can successfully predict the microstructure of solidified casting. The relationship between the microstructure and the macroscopic behavior of the alloy are analyzed quantitatively and qualitatively. The relationship between the SDAS and cooling rate is $\lambda_2 = 76.4747(GV)^{-0.2926}$. The microhardness tends to decrease along the axial direction.
3. With the increase of solidification rate, the response behavior of secondary dendrite arms spacing (SDAS) is sensitive to the change of solidification parameters. The SDAS of GTD-222 Ni-based superalloy transforms from a dendritic structure to cellular growth for the increasement of the temperature gradient.
4. A novel high-efficiency experiment method is proposed to reproduce the conventional casting conditions by the prior model of the numerical simulation and the physical simulation, which can be also applied to other casting studies of all kinds for the enhancement of time- and cost-saving.

Acknowledgments This work was financially supported by The Major State Basic Research Development Program of China (2016YFB0701405) and National Natural Science Foundation of China (51705314, 51771118, 51821001, U1760110). The authors gratefully acknowledge the financial supports from the National Industrial Basis Improvement Project under Project (TC160A310-12-1), The 13th Five-year Major Project of Aero Engine and Gas Turbine of China (2017-VII-008) and Startup Fund for Youngman Research at SJTU (18X100040025).

References

1. Chang HC, Lin A (2005) Automatic inspection of turbine blades using a 3-axis CMM together with a 2-axis dividing head. *Int J Adv Manuf Technol* 26(7-8):789–796
2. Jahangiri MR, Abedini M (2014) Effect of long time service exposure on microstructure and mechanical properties of gas turbine vanes made of IN939 alloy. *Mater Des* 64:588–600
3. Zheng L, Zhang G, Lee TL, Gorley MJ, Wang Y, Xiao C, Li Z (2014) The effects of Ta on the stress rupture properties and microstructural stability of a novel Ni-base superalloy for land-based high temperature applications. *Mater Des* 61:61–69
4. Seaver DW, Beltran AM (1993) Nickel-Base Alloy GTD-222, a new gas turbine nozzle Alloy. *J Eng Gas Turbines Power* 115(1): 155–159
5. Wang R, Wang W, Zhu G, Pan W, Zhou W, Wang D, Li F, Huang H, Jia Y, Du D (2018) Microstructure and mechanical properties of the TiN particles reinforced IN718C composite. *J Alloys Compd* 762: 237–245
6. Kartavykh AV, Tcherdyntsev VV, Gorshenkov MV, Kaloshkin SD (2014) Microstructure engineering of TiAl-based refractory intermetallics within power-down directional solidification process. *J Alloys Compd* 586:S180–S183
7. Aveson JW, Tennant PA, Foss BJ, Shollock BA, Stone HJ, Souza ND (2013) On the origin of sliver defects in single crystal investment castings. *Acta Mater* 61(14):5162–5171
8. Li WP, Yong G, Wen LG, Zhi LH, Hu Z (2010) Prediction of shrinkage porosity (hole) in tial based alloy blade and its processing optimization based on the ProCAST. *Spec Cast Nonferrous Alloys* 30(06):504–507 + 592
9. Yang L, Chai LH, Liang Y, Zhang Y, Bao CL, Liu SB, Lin J (2015) Numerical simulation and experimental verification of gravity and centrifugal investment casting low pressure turbine blades for high Nb-TiAl alloy. *Intermetallics* 66:149–155

10. Eriksson M, Wikman B, Bergman, G (2003) Estimation of material parameters at elevated temperatures by inverse modeling of a Gleeble experiment. IUTAM symposium on field analyses for determination of material parameters-experimental and numerical aspects. Springer Netherlands. https://doi.org/10.1007/978-94-010-0109-0_14
11. Lewandowski MS, Overfelt RA (1999) High temperature deformation behavior of solid and semi-solid alloy 718. *Acta Mater* 47(18): 4695–4710
12. Rahimian M, Milenkovic S, Sabirov I (2013) Microstructure and hardness evolution in MAR-M247 Ni-based superalloy processed by controlled cooling and double heat treatment. *J Alloys Compd* 550:339–344
13. Fisher DJ (1986) Fundamentals of solidification. *Trans Tech. Pub.* 1989
14. Zhai W, Geng DL, Wang WL, Wei B (2012) A calorimetric study of thermodynamic properties for binary Cu-Ge alloys. *J Alloys Compd* 535:70–77
15. Rahimian M, Milenkovic S, Maestro L, Sabirov C (2015) Physical Simulation of Investment Casting of Complex Shape Parts[J]. *Metall Mater Trans A* 46(5):2227–2237
16. Cao S, Gu D, Shi Q (2017) Relation of microstructure, microhardness and underlying thermodynamics in molten pools of laser melting deposition processed TiC/Inconel 625 composites. *J Alloys Compd* 692:758–769
17. Chen W (2018) High-efficiency computing for accelerated materials discovery. In: Shin D, Saal J (eds) *Computational Materials System Design*. Springer, Cham, pp 169–191
18. Makihata M, Pisano AP (2019) High-efficiency microstructure printing technology using inflatable thin membrane with microchannel. *Int J Adv Manuf Technol* 103:1709–1719. <https://doi.org/10.1007/s00170-019-03672-8>
19. Kirklin S, Saal JE, Hegde V, Wolverson CM (2016) High-efficiency computational search for strengthening precipitates in alloys. *Acta Mater* 102:125–135
20. Safran G (2018) “One-sample concept” micro-combinatory for high efficiency TEM of binary films. *Ultramicroscopy* 187:50–55
21. Li J, Wang B, Qin Y, Fang S, Huang X, Chen P (2019) Investigating the effects of process parameters on the cross wedge rolling of TC6 alloy based on temperature and strain rate sensitivities. *Int J Adv Manuf Technol* 103:2563–2577. <https://doi.org/10.1007/s00170-019-03461-3>
22. Bor HY, Wei CN, Jeng RR, Ko PY (2008) Elucidating the effects of solution and double aging treatment on the mechanical properties and toughness of MAR-M247 superalloy at high temperature. *Mater Chem Phys* 109(2):334–341
23. Chen J, Lee JH, Jo CY, Choe SJ, Lee YT (1998) MC carbide formation in directionally solidified MAR-M247 LC superalloy. *Mater Sci Eng A* 247(1):113–125
24. Whitesell HS, Li L, Overfelt RA (2000) Influence of solidification variables on the dendrite arm spacings of Ni-based superalloys. *Metall Mater Trans B Process Metall Mater Process Sci* 31(3): 546–551
25. Kostic S, Golubovic A, Valcic A (2009) Primary and secondary dendrite spacing of Ni-based superalloy single crystals. *J Serb Chem Soc* 74(1):61–69
26. Liu C, Shen J, Zhang J, Lou L (2010) Effect of withdrawal rates on microstructure and creep strength of a single crystal superalloy processed by LMC. *J Mater Sci Technol* 26(4):306–310
27. Franke MM, Hilbinger RM, Konrad C, Glatzel U, Singer RF (2011) Numerical determination of secondary dendrite arm spacing for IN738LC investment castings. *Metall Mater Trans A* 42(7):1847–1853
28. Zhang Y, Huang B, Li J (2013) Microstructural evolution with a wide range of solidification cooling rates in a Ni-based superalloy. *Metall. Mater. Trans. A* 44(4):1641–1644
29. Souza ND, Ardakani MG, Wagner A, Shollock BA, Lean MMC (2002) Morphological aspects of competitive grain growth during directional solidification of a nickel-base superalloy, CMSX4. *J Mater Sci* 7:481–487
30. Das D, Pratihari DK, Roy GG (2018) Cooling rate predictions and its correlation with grain characteristics during electron beam welding of stainless steel. *Int J Adv Manuf Technol* 97:2241
31. Bemani M, Pouranvari M (2019) Resistance spot welding of Nimonic 263 nickel-based superalloy: microstructure and mechanical properties. *Sci Technol Weld Joining*. 1-9
32. Melo MLN, Penhalber CL, Pereira NA, Pellicciari CL, Santos CA (2007) Numerical and experimental analysis of microstructure formation during stainless steels solidification. *J Mater Sci* 42(7): 2267–2275dd

Publisher's note Springer Nature remains neutral with regard to jurisdictional claims in published maps and institutional affiliations.